

Practical Cell Design for PTMA-Based Organic Batteries: an Experimental and Modeling Study

Alessandro Innocenti, Isaac Álvarez Moisés, Olivera Lužanin, Jan Bitenc, Jean-François Gohy, and Stefano Passerini*

Cite This: <https://doi.org/10.1021/acsami.3c11838>

Read Online

ACCESS |

Metrics & More

Article Recommendations

Supporting Information

ABSTRACT: Poly(2,2,6,6-tetramethyl-1-piperidinyloxy methacrylate) (PTMA) is one of the most promising organic cathode materials thanks to its relatively high redox potential, good rate performance, and cycling stability. However, being a p-type material, PTMA-based batteries pose additional challenges compared to conventional lithium-ion systems due to the involvement of anions in the redox process. This study presents a comprehensive approach to optimize such batteries, addressing challenges in electrode design, scalability, and cost. Experimental results at a laboratory scale demonstrate high active mass loadings of PTMA electrodes (up to 9.65 mg cm^{-2}), achieving theoretical areal capacities that exceed 1 mAh cm^{-2} . Detailed physics-based simulations and cost and performance analysis clarify the critical role of the electrolyte and the impact of the anion amount in the PTMA redox process, highlighting the benefits and the drawbacks of using highly concentrated electrolytes. The cost and energy density of lithium metal batteries with such high mass loading PTMA cathodes were simulated, finding that their performance is inferior to batteries based on inorganic cathodes even in the most optimistic conditions. In general, this work emphasizes the importance of considering a broader perspective beyond the lab scale and highlights the challenges in upscaling to realistic battery configurations.

KEYWORDS: PTMA, cost, modeling, polymer battery, organic battery

Practical cell design for PTMA-based organic batteries: an experimental and modeling study

Lab-scale experimental results



{ = 10 mg cm^{-2} PTMA organic electrode
= 1 mAh cm^{-2}
= $3.6 \text{ V vs. Li/Li}^+$

Modeling of upscaling



{ Dual-ion battery operation?
Realistic cell design?
Cost and energy density?

1. INTRODUCTION

As the demand for lithium-ion batteries continues to surge with the increasing adoption of electric vehicles and the integration of renewable energy sources,¹ concerns regarding the availability and affordability of essential raw materials have emerged. Projections of the capacity required to achieve full electrification of transportation and to support photovoltaic and wind power plants over the next three decades raise concerns regarding the strains on battery supply chains.^{2,3} The upward trajectory of raw material prices observed in recent years further highlights the urgency of exploring alternatives that leverage readily available and more uniformly distributed resources while maintaining a comparable performance.

In response to these challenges, researchers have actively investigated various chemistries as potential alternatives to lithium-ion batteries,^{4,5} among which organic batteries appear promising due to their use of abundant and renewable carbon-based compounds.^{6–8}

Organic electrode materials can be classified as either n-type or p-type involving the reversible uptake of cations or anions, respectively.^{9,10} N-type materials generally have lower average voltage, slower kinetics, and higher specific capacity compared to p-type materials, and their redox mechanism is analogous to

that of commercial lithium-ion anodes and cathodes. Instead, in p-type materials, the electrochemical reaction generally occurs at a relatively high potential (3.5–4.5 V) due to their interaction with anions, which makes them suitable for coupling with alkali metal anodes or carbonaceous anode materials with low intercalation potential, resulting in high-voltage cells.^{11,12} Such batteries operate in a dual-ion configuration, where the anode and cathode interact with cations and anions, respectively.¹³ As a result, batteries based on p-type materials differ from typical lithium-ion batteries because the electrolyte plays a crucial role as a source of anions in the redox reaction.¹⁴

Among p-type materials, poly(2,2,6,6-tetramethyl-1-piperidinyloxy methacrylate) (PTMA) is probably the most prominent one. Being the polymerized form of the stable radical 4-methacryloyloxy-2,2,6,6-tetramethylpiperidin-1-oxyl (TEMPO-methacrylate), it shows excellent rate capabilities and a stable,

Special Issue: Organic Battery Materials

Received: August 10, 2023

Accepted: September 22, 2023

plateau-like redox potential at around 3.6 V vs Li/Li⁺.^{15,16} First reported in 2002 by Nishide et al.,¹⁷ it has been the subject of many studies focusing on its mechanistic behavior,^{18–21} electrochemical properties,^{22–25} and the development of PTMA-based organic batteries.^{26–29} Several strategies to stabilize this polymer against dissolution in the electrolyte and to improve its very poor electronic conductivity have been proposed and implemented, resulting in the development of electrodes with relevant active material mass loadings.^{30–32}

In fact, for PTMA-based batteries (and organic batteries in general) to compete with conventional lithium-ion systems, it is crucial to maximize the areal capacity (and hence the active material mass loading) while maintaining a good cycling stability and rate performance, with the additional challenge of the intrinsic low density of polymers, which results in very thick electrodes when compared with inorganic-based systems at the same mass loadings.³³ Thus, it is fundamental to consider a broader perspective beyond the results obtained from laboratory-scale batteries. Scaling up the system often reveals significant challenges that may not be apparent at small scales. For example, the redox mechanism involving anions, which is a peculiar characteristic of PTMA, has a profound influence on the practical design of PTMA-based batteries, due to the above-mentioned crucial role of the electrolyte. Surprisingly, this aspect remains relatively unexplored in the existing literature.

In this study, we present a comprehensive approach that covers various aspects, including optimizing the type and quantity of carbon additive in the electrode and maximizing the active mass loading at a lab-scale, simulating the behavior of PTMA-Li metal batteries based on the experimental results through physical modeling to evaluate the influence of design parameters, and conducting a detailed cost and energy analysis for these batteries. With this systematic methodology, we shed light on the challenges of transferring good battery materials research from typical laboratory conditions to practical cell configuration.

2. MATERIALS AND METHODS

2.1. Active Material Synthesis. The mixture of poly(2,2,6,6-tetramethyl-1-piperidinyloxy methacrylate) (PTMA) and conductive carbon additives was synthesized via the melt polymerization method described in Vlad et al.³⁰ The amount of carbon additive added during the synthesis x (in grams) is equal to its weight fraction in the mixture multiplied by 20.

In a typical synthesis, $20-x$ g of 2,2,6,6-tetramethyl-4-piperidyl methacrylate (TMPM 98%, TCI) and $6.765 \cdot (20-x)$ mg of azobis(isobutyronitrile) (AIBN, recrystallized in ethanol, TCI) were dissolved in acetone (VWR, technical grade). Subsequently, $30.59 \cdot (20-x)$ μ L of ethylene glycol dimethacrylate (EGDME 98%, Acros Organics) as a cross-linking agent was added to the solution. The solvent was removed by evaporation in a rotary evaporator and then in a Schlenk line connected to a vacuum pump equipped with a nitrogen trap.

The resulting dried precursor mixture was placed in a ball mill apparatus (Type S1, Retsch GmbH) containing three agate balls with a diameter of 3 cm. Additionally, x g of conductive carbon additive was added to the mixture. The precursor mixture was ball-milled for 1 h at 80% of the maximum speed. Subsequently, the milled mixture was transferred to a 1000 mL cylindrical glass reactor, which underwent three purges with argon gas. The reactor was then immersed in a stirred oil bath and kept at 80 °C overnight to facilitate the polymerization reaction.

After cooling to room temperature, the product, poly(2,2,6,6-tetramethyl-1-piperidyl methacrylate) (PTMPT) mixed with a carbon additive, was extracted by the reactor. Swelling it with dichloromethane

(DCM, technical grade, VWR) allowed for the removal of the product, which was subsequently washed with the same solvent. The polymer-carbon mixture was dried using a rotary evaporator and a vacuum pump, followed by ball milling for 1 h at 80% of the maximum speed of the ball mill apparatus.

To oxidize the PTMPT, 20 g of the polymer-carbon mixture was dispersed in methanol (technical grade, VWR) within a 1000 mL round-bottom glass reactor. Stirring the mixture with a magnetic bar, $0.2729 \cdot (20-x)$ g of sodium tungstate (Na₂WO₄ 99%, Sigma-Aldrich), $0.1765 \cdot (20-x)$ g of ethylenediaminetetraacetic sodium salt (EDTA 98.5%, Sigma-Aldrich), and $2 \cdot (20-x)$ mL of a 30% aqueous solution of hydrogen peroxide (H₂O₂, Sigma-Aldrich) were added. The reaction took place for 48 h in a stirred oil bath at 60 °C accompanied by an air-cooled reflux condenser. The resulting mixture was filtered several times under vacuum using a 1:1 volume ratio solution of water and methanol, until the washing solution became colorless. The obtained mixture was dried in a vacuum oven (Binder) at 60 °C overnight and further ball-milled for 1 h at 80% of the maximum speed of the ball mill apparatus.

The synthesized samples had the following composition (in weight fractions):

- **PTMA-GN15:** 85% PTMA, 15% graphene nanoplatelets (2–10 nm, Thermo Scientific)
- **PTMA-SP15:** 85% PTMA, 15% carbon black (Super P, IMERYS)
- **PTMA-MW15:** 85% PTMA, 15% multiwalled carbon nanotubes (NC7000, Nanocyl)
- **PTMA-MW10:** 90% PTMA, 10% multiwalled carbon nanotubes
- **PTMA-MW5:** 95% PTMA, 5% multiwalled carbon nanotubes
- **PTMA-MW2.5:** 97.5% PTMA, 2.5% multiwalled carbon nanotubes

2.2. Electrode Preparation. For the preparation of PTMA-based electrodes, a water-based method was employed. In a typical preparation, the following components were combined: 900 mg of the polymer-carbon mixture, 50 mg of conductive carbon (Super C45, IMERYS), 30 mg of carboxymethyl cellulose from a 3% weight aqueous solution (CMC, Walocel CRT 2000 PPA 12), 20 mg of styrene-butadiene rubber from a 40% latex solution (SBR, Zeon BM451-B), and 500 mg of deionized water (solid/solvent weight ratio: 40/60). To ensure thorough mixing, the components were blended in a planetary centrifugal mixer (ARE-250, THINKY) at 2000 rpm for 10 min. The weight ratio of the electrode components was maintained at 90:5:3:2 (PTMA/MWCNT:C45:CMC:SBR). Subsequently, the mixture was coated onto a carbon-coated aluminum foil (Wellcos) with a wet thickness of 120 μ m for the low mass loading electrodes or 300 μ m for the high mass loading ones. The slurry-coated foil was then dried overnight in a dry room with a dew point below –70 °C. Electrodes with a diameter of 12 mm (or 18 mm, for the impedance tests) were cut and pressed with a force of 1 ton. These electrodes were further dried at 80 °C for 12 h in a Büchi oven connected to a vacuum pump, maintaining a pressure below 1×10^{-3} mbar. Finally, the dried electrodes were transferred to an argon-filled glovebox (MB200B ECO, MBraun) with oxygen and water content below 0.1 ppm.

2.3. Physicochemical Characterization. The thermogravimetric analysis (TGA) was performed with a TG 209 F1 Libra instrument (NETZSCH GmbH). All the tests were performed with a heating rate of 5 K min^{–1} with a total gas flow of 40 mL min^{–1}. Alumina open crucibles (65 μ L) were filled with 10 ± 0.010 mg of sample. The weight loss in the charts is reported in mass because each crucible was filled with the same amount of material; hence, in this situation the percentage and the weight loss in this case are totally comparable. The conductive carbon additives were analyzed with the same experimental procedure, too, and in this case, the crucibles were filled with the amount of carbon additive that should be present in 10 mg of the respective polymer-carbon mixture (e.g., for the comparison with PTMA-MW15, the mass of multiwalled carbon nanotubes in the crucible was 1.5 mg). The first part of the test (pyrolysis) used only nitrogen gas, heating to 800 °C. After cooling back to 30 °C, the gas was

Table 1. Physicochemical Characterization of the Powders of PTMA-Carbon Composites

Sample	Additive	Theoretical powder composition ^a	Actual powder composition ^b	Powder true density (g cm ⁻³)	Powder electronic conductivity (S cm ⁻¹)
PTMA-GN15	Graphene nanoplatelets	85/15	83.57/15.42/1.01	1.2616 ± 0.0001	(4.8 ± 0.2) × 10 ⁻³
PTMA-SP15	Carbon black	85/15	82.72/16.54/0.74	1.2383 ± 0.0001	(1.5 ± 0.3) × 10 ⁻⁷
PTMA-MW15	Multiwalled carbon nanotubes	85/15	83.45/13.56/2.99	1.2660 ± 0.0002	(5.1 ± 0.5) × 10 ⁻²
PTMA-MW10	Multiwalled carbon nanotubes	90/10	87.60/10.10/2.30	1.2265 ± 0.0004	(7.1 ± 0.8) × 10 ⁻³
PTMA-MW5	Multiwalled carbon nanotubes	95/5	92.63/5.38/1.99	1.1930 ± 0.0001	(5.8 ± 0.6) × 10 ⁻⁷
PTMA-MW2.5	Multiwalled carbon nanotubes	97.5/2.5	95.06/2.94/2.00	1.1794 ± 0.0001	-

^aPolymer/conductive additive weight ratio. ^bPolymer/conductive additive/impurities weight ratio.

switched to a mixture of 5% oxygen and 95% nitrogen (volume fraction), and the temperature was kept constant for 30 min. Then, in the second part of the test (oxidation) the sample was heated to 800 °C for the samples with multiwalled carbon nanotubes or 1000 °C for the samples with graphene nanoplatelets and carbon black.

The true density of the samples was measured with a helium pycnometer (Ultrapyc 1200e, Quantachrome Instruments) at room temperature.

The scanning electron microscopy (SEM) images of the powders and electrodes were taken with a ZEISS Crossbeam XB340 instrument at a working voltage of 5 kV.

2.4. Electrochemical Characterization. The electronic conductivity of the samples was measured with the two-contact probe method. The powder samples were mixed with polytetrafluoroethylene (PTFE) binder, in a weight ratio of 9:1 in a dispersion of isopropanol. Mixtures were subjected to ball milling on a Retsch PM100 for 30 min (300 rpm). Black gum-like slurries were then rolled between parchment paper and glass plate and left to dry in vacuum overnight. For each sample, three pellets were prepared, containing 50, 100, 200 mg, and/or 400 mg of active material, and they were pressed with 4 ton for 1 min. The diameters of all of the pellets were 10 mm. After drying in a vacuum oven, conductive adhesive silver paste was applied on both sides of the pellet, and the pellet was dried once more in a vacuum oven overnight at 80 °C. The thickness of all samples was measured after drying with a micrometer. For the impedance measurement, the pellets were put between two copper foils that were connected to the impedance analyzer. All the impedance measurements were conducted on a VMP Bio-Logic Instrument in the frequency range from 1 MHz to 10 mHz at 25 °C. The resistance found at the crossing of the real axis was used as the resistance value for the sample. Three pellets for each sample with different thicknesses were measured, and the slope of the resistance-thickness chart was obtained through linear regression. This slope k was used in the formula

$$\sigma = \frac{1}{k} \frac{1}{A} \quad (1)$$

where A is the area of the pellet, to calculate the electronic conductivity σ . The charts with the results of the resistance measurements on all of the pellets are shown in Figure S1. With PTMA-MW2.5, it was not possible to obtain meaningful results, probably due to its strongly insulating behavior.

The galvanostatic charge/discharge tests were performed in a two-electrode coin cell setup, using a 12 mm diameter PTMA-based cathode, a 16 mm diameter glass fiber separator (Whatman GF/A) normally soaked with 70 μ L of 1 M LiPF₆ or 1 M lithium bis(fluorosulfonyl)imide (LiFSI) in 1:1 ethyl carbonate (EC)/dimethyl carbonate (DMC) 1:1 (battery grade, BASF Selectylite), and a 14 mm diameter lithium metal anode (500 μ m, battery grade, Honjo). For the tests, 10 μ m thick polyolefin Hipore SV718 (Asahi Kasei) separators with 16 mm diameter were employed, which were left overnight in a vial with the above-mentioned electrolytes and then used after removing the excess electrolyte on the surface. An additional drop of electrolyte was added on the cathode surface to fill the electrode porosity. For the tests with sodium metal (99.8%, Acros Organics) a 14 mm anode was used,

and the electrolyte was 1 M NaPF₆ (battery grade, Fluorochem) dissolved in EC (battery grade, UBE)/PC (battery grade, UBE) 3:7. The cells, hosted in climatic chambers (Binder) at 20 °C, were tested with a Maccor Series 4000 battery cycler between 3 and 4 V (2.8 and 3.8 V for the tests with sodium metal). The specific capacity used to calculate the current was 111 mAh g⁻¹, and the active material mass of the electrodes was calculated by using the theoretical weight fraction of PTMA in the electrode. The cells performed 3 cycles at 0.1C, 5 cycles at 0.2C, 0.5C, 1C, 2C, 5C, 10C, and 25C, and then they cycled at 1C until the end of the test.

The electrochemical impedance spectroscopy (EIS) tests were conducted by using a three-electrode ECC-PAT-Core cell (EL-CELL GmbH) setup. The cathode consisted of an 18 mm diameter PTMA-based electrode. The separator was made of glass fiber (Whatman GF/A) with a diameter of 21 mm, soaked in 200 μ L of the electrolyte solution. An 18 mm diameter lithium metal disk (500 μ m, battery grade, Honjo) served as the anode, and a lithium-coated nickel ring (EL-CELL GmbH) acted as the reference electrode, positioned between the cathode and the separator. The EIS measurements were carried out at a temperature of 20 °C in climatic chambers (Binder) using a Biologic VMP battery cycler equipped with a frequency response analyzer. The EIS tests were executed in the potentiostatic mode, covering a frequency range of 100 kHz to 100 mHz, with 10 points for each decade. The voltage amplitude for EIS measurements was set at 10 mV. Galvanostatic charge–discharge tests were also performed with the same setup, instrument, and conditions, together with the EIS measurements. The cells performed 3 cycles at 0.1, then 3 cycles at 0.2C, 0.5C, 1C, 2C, and 5C, followed by 20 cycles at 1C. This whole procedure was repeated two times, with the impedance measurements made each time before the 0.2C cycles, measuring 10 impedance spectra at different state of charge (SOC) points along the 0.1C discharge that preceded the 0.2C cycles.

2.5. Physical Model. The physical model, presented in a previous work,³⁴ is composed of the equations presented in Table S1. The model simulated the behavior of a dual-ion battery, i.e., a battery with a cathode where anions partake in the redox process and an anode where cations are instead involved, with a modified version of the pseudo-2D Doyle-Fuller-Newman model for the macroscale physical simulation of lithium-ion batteries. The cathode is a porous electrode, while the anode is modeled as a metal surface, and the electrodes are separated by a porous separator. The model is implemented in COMSOL Multiphysics, in version 6.0, using the Battery Design Module. More details are given in the Supporting Information.

2.6. Cost and Performance Analysis Model. An analysis of the energy density and cost was conducted using a modified version of the freely available software BatPaC 5.0, which is described in detail in a report published by the Argonne National Laboratory.³⁵ This software model is specifically designed to simulate battery packs with predetermined energy and power ratings. It considers the costs associated with various components, such as active materials, conductive carbon, binders, separators, electrolytes, current collectors, casings, pack current collectors, cooling systems, labor, and overhead expenses. Furthermore, it considers the investment costs related to the production site.

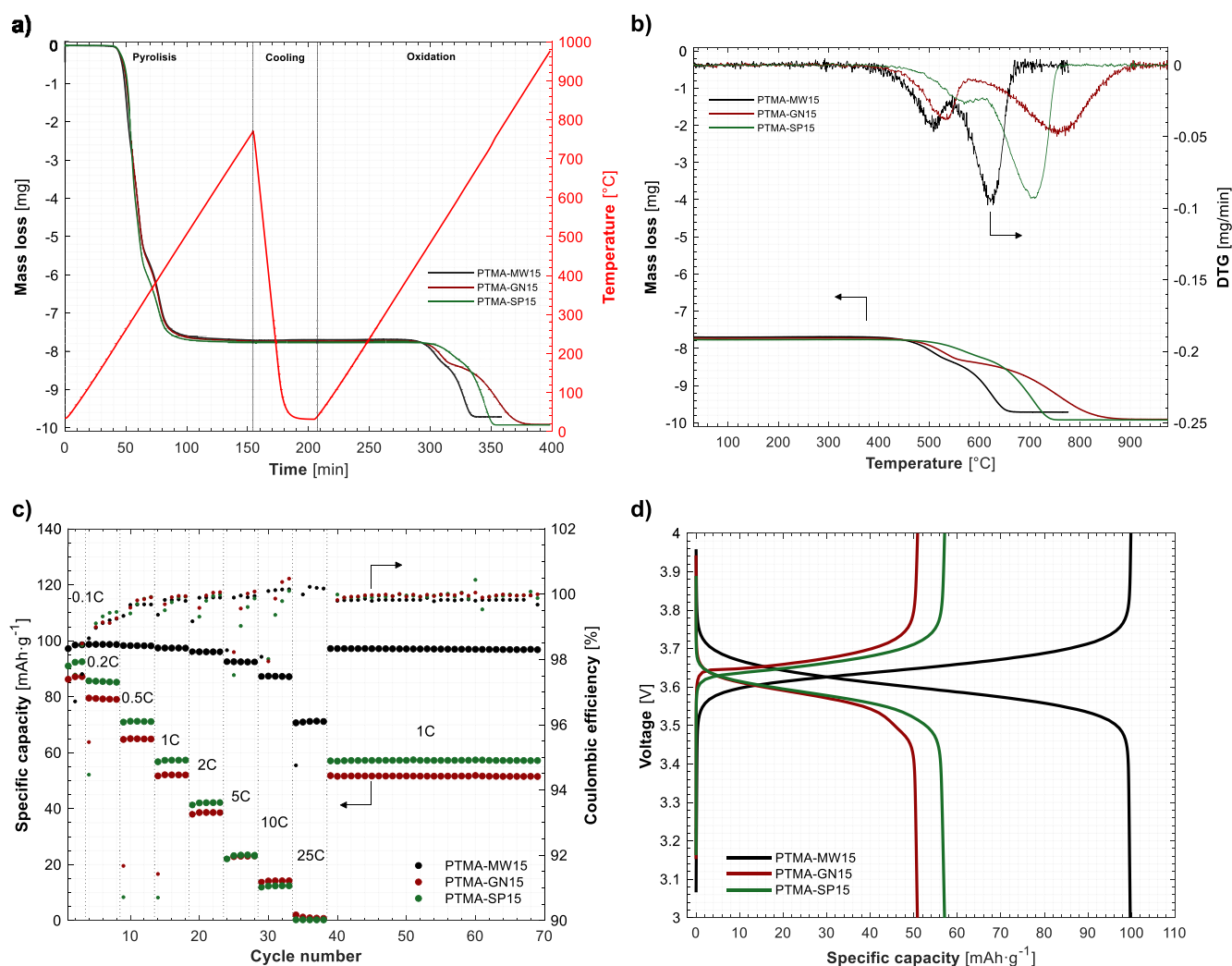


Figure 1. (a) TGA results of the PTMA-MW15, PTMA-GN15, and PTMA-SP15 samples. (b) Detail on the oxidation part of the TGA results on the three samples, with the respective DTG curves. (c) Specific capacity and Coulombic efficiency vs cycle number for the rate performance test of the three samples in coin cells with a lithium metal anode at 20 °C. (d) Related voltage vs specific capacity charge and discharge curves of the three samples at 1C (cycle no. 50 in panel c).

The simulated battery pack is intended for application in domestic energy storage, featuring a power rating of 7 kW and an energy rating of 11.5 kWh. Each pack consists of 36 cells within a module, resulting in a total of 72 cells organized in a series of 2 modules. The production volume is established at 4 347 800 packs per year, corresponding to a yearly production capacity of about 50 GWh.

3. RESULTS AND DISCUSSION

3.1. Experimental Results. Increasing the active material mass loading and accordingly the usable areal capacity entails having the smallest possible amount of conductive carbon in the final electrode. Hence, choosing an additive that can ensure good electrochemical performance when combined with PTMA while keeping its amount as low as possible is a crucial step in electrode optimization. We synthesized then three batches with different conductive carbons added during the synthesis process, i.e., multiwalled carbon nanotubes (PTMA-MW15), graphene nanoplatelets (PTMA-GN15), and carbon black (PTMA-SP15). The weight fraction of additive with respect to the precursor was fixed to 15% for all three batches. The results of the physicochemical characterization of these samples are reported in Table 1.

The synthesized batches were analyzed with TGA, using a two-step procedure: a pyrolysis in inert gas (N_2) up to 800 °C followed by a cooldown period and oxidation in 5% O_2 and 95% N_2 up to 800 °C, for the sample with multiwalled carbon nanotubes, or 1000 °C, for the other samples. The pyrolysis step induces the decomposition of the polymeric part, as evident from the sharp decline in the sample mass observed in Figure 1a at around the 40 min mark (220 °C) for all the samples. Most of the decomposition products are gases which leave the crucible, but a minor fraction of the polymer decomposes into pyrolysis soot, i.e., carbonaceous particles.³⁶ Hence, the mass loss during the pyrolysis is not equal to the polymer weight fraction since a small but relevant part remains as a solid product. Therefore, the oxidation step is required to burn off the carbon species remaining in the sample, which will be a mixture of pyrolysis soot and a conductive carbon additive.

The TGA confirmed the decomposition of two distinct components, polymer and conductive carbon, in a relative weight ratio comparable to that of the one set during synthesis (Figure 1b). In fact, we can see how the derivative of the mass loss (DTG) during the oxidation phase shows two peaks for all the studied samples (Figure S2a–c). The peak at lower

Table 2. Physicochemical Characterization of PTMA-Carbon Composite Electrodes

Sample	Theoretical electrode composition ^a	Actual electrode composition ^b	Electrode mass loading (mg cm ⁻²)	Electrode density (g cm ⁻³) ^c	Electrode porosity (%) ^c
PTMA-GN15	76.5/13.5/5/5	75.2/13.9/5/5/0.9	4.44 ± 0.21	0.788 ± 0.025	38.66 ± 1.35
PTMA-SP15	76.5/13.5/5/5	74.4/14.9/5/5/0.7	4.06 ± 0.21	0.689 ± 0.007	45.46 ± 1.35
PTMA-MW15	76.5/13.5/5/5	75.1/12.2/5/5/2.7	4.09 ± 0.22	0.787 ± 0.017	37.91 ± 1.35
			8.40 ± 0.32 ^d	-	-
			9.01 ± 0.53 ^e	-	-
PTMA-MW10	81/9/5/5	78.9/9.1/5/5/2.0	3.79 ± 0.07	0.727 ± 0.015	41.62 ± 1.18
PTMA-MW5	85.5/4.5/5/5	83.4/4.8/5/5/1.8	4.12 ± 0.05	0.746 ± 0.017	39.10 ± 1.37
PTMA-MW2.5	87.75/2.25/5/5	85.6/2.6/5/5/1.8	4.28 ± 0.12	0.738 ± 0.004	39.28 ± 0.35

^aPolymer/conductive additive/C45/binder weight ratio. ^bPolymer/conductive additive/C45/binder/impurities weight ratio. ^cThe density and porosity measurements were done on other electrodes than the ones used for the electrochemical characterization, prepared in the same conditions and with the same parameters. ^dMass loading of electrodes obtained increasing the coating wet thickness from 120 to 300 μm. ^eMass loading of electrodes obtained increasing the coating wet thickness from 120 to 300 μm and the solid weight fraction in the slurry from 40% to 45%

temperature can be associated with the oxidation of the pyrolytic soot formed by the polymer pyrolysis during the first phase of the TGA test in inert atmosphere,³⁶ while the second peak can be assigned to the combustion of the conductive additive. In fact, when performing the same TGA test on the sole conductive carbon additives, the oxidation DTG peaks of multiwalled carbon nanotubes and graphene nanoplatelets correspond with the second DTG peak of the respective polymer-carbon mixtures. The carbon black oxidation peak has the same shape of the second DTG peak of PTMA-SP15, but shifted to ≈80 °C, as the heat released by the preceding oxidation of the pyrolysis soot may decrease the activation energy for the carbon black oxidation. By measuring the mass loss of each sample up to the point where the DTG has a maximum between the two peaks, it is possible to estimate the amount of polymer present in the mixture by summing the mass loss due to the pyrolysis and the one due to the oxidation of the pyrolytic soot derived from the polymer. Moreover, the residual mass at the end of the oxidation indicates the amount of nonvolatile impurities that are present in the samples due to the synthesis process, hence giving a more accurate representation of the composition of the mixture. The weight fraction of PTMA resulting from the TGA curves is about 1.5–2.5% lower than the theoretical one, probably due to a small fraction of nonpolymerized monomer after the first synthesis step which was washed away.

The true density of the samples was measured via helium pycnometry, and the results were 1.266 g cm⁻³ for PTMA-MW15, 1.262 g cm⁻³ for PTMA-GN15, and 1.238 g cm⁻³ for PTMA-SP15. The lower value for the latter sample can be associated with the low true density of carbon black (1.83 g cm⁻³) when compared to graphene nanoplatelets (2.26 g cm⁻³).³⁷ Despite having PTMA-MW15 the largest true density value, the true density of the multiwalled carbon nanotubes is actually assumed to be even slightly lower than the other additives (1.75 g cm⁻³).³⁷ However, the lower amount of carbon and higher amount of high-density metal oxide impurities in PTMA-MW15 compared to the other two samples explain this discrepancy. It is worth to note that the density of these active materials is around one-third of lithium iron phosphate (3.45 g cm⁻³) and one-fourth of lithium layered oxides (>4.5 g cm⁻³),³⁵ due to the light organic elements of which they are made of, and this comes as a disadvantage for the volumetric capacity of PTMA-based batteries.

The electronic conductivity of the electrode materials, measured through impedance spectroscopy, shows how the most conductive sample is PTMA-MW15, with a value of 5.1 ×

10⁻² S cm⁻¹. The multiwalled carbon nanotubes are known to form good percolation networks for the electron conduction thanks to their high aspect ratio (≈160),³⁸ leading to a relatively high value for the electronic conductivity. Note that the solid-state electronic conductivity of PTMA is estimated to be in the 10⁻¹¹ S cm⁻¹ order of magnitude,³⁹ with only very pure nanometer-thick PTMA films that reach 10⁻⁵ S cm⁻¹.⁴⁰ The benefits of using high aspect ratio conductive additives for radical polymer batteries was also confirmed by studies that employed vapor-grown carbon fibers (VGCF) during the electrode preparation.^{31,41,42} Significant improvements of the performance of PTMA-based cathodes were already observed with carbon nanotubes and reduced graphene oxide.^{43,44} The graphene nanoplatelets, showing lower aspect ratios (10–100 range even in the same sample due to agglomeration and stacking of the nanoplatelets,⁴⁵ therefore a lower value of 4.8 × 10⁻³ S cm⁻¹ is measured. The aspect ratio of carbon black has a value close to unity due to its quasi-spherical shape. Hence, the formation of a percolation network with this additive is severely hindered, achieving only a limited electronic conductivity of 1.5 × 10⁻⁷ S cm⁻¹.⁴⁶

SEM images of the powders and electrodes are in accordance with the electronic conductivity measurements. In fact, the images of PTMA-SP15 powder and electrode show charging effects, indicating the presence of isolated nonconductive polymer agglomerates in the analyzed materials (Figure S3). Regarding the PTMA-GN15 electrode images, some insulating polymer particles can be also individuated but not in the powder sample (Figure S4). Such features are not observed, however, in the images of PTMA-MW15 powder and electrodes (Figure S5).

The composition, mass loading, density, and porosity of the electrodes are reported in Table 2. The active material mass loadings are above 4 mg cm⁻². The electrode density of PTMA-GN15 and PTMA-MW15 is almost equal (respectively, 0.788 and 0.787 g cm⁻³) while the one of PTMA-SP15 is significantly lower (0.689 g cm⁻³), resulting in a porosity of around 38% for the first two samples and around 45% for the latter (see the Supporting Information for the details about the calculations). The values are relatively high for battery electrodes, which usually lie in the 20–30% range,⁴⁷ but since PTMA-based cathodes require a high amount of electrolyte due to the involvement of anions in the electrochemical reaction, larger and more numerous pores can be beneficial for a properly working electrode.

Table 3. Electrochemical Characterization of Selected PTMA-Carbon Composite Electrodes

Sample	Active material mass loading	Theoretical specific capacity/ areal capacity/volumetric capacity	Specific capacity/areal capacity/ volumetric capacity @0.2C (discharge)	Specific capacity/areal capacity/ volumetric capacity @1C (discharge)	Specific capacity/areal capacity/volumetric capacity @ 5C (discharge)
PTMA-GN15	4.38 mg cm ⁻²	111 mAh g ⁻¹ /0.486 mAh cm ⁻² /66.9 mAh cm ⁻³	79.2 mAh g ⁻¹ /0.347 mAh cm ⁻² /47.7 mAh cm ⁻³	52.1 mAh g ⁻¹ /0.228 mAh cm ⁻² /31.4 mAh cm ⁻³	23.3 mAh g ⁻¹ /0.102 mAh cm ⁻² /14.1 mAh cm ⁻³
PTMA-SP15	4.20 mg cm ⁻²	111 mAh g ⁻¹ /0.466 mAh cm ⁻² /68.5 mAh cm ⁻³	85.3 mAh g ⁻¹ /0.358 mAh cm ⁻² /45.0 mAh cm ⁻³	57.4 mAh g ⁻¹ /0.241 mAh cm ⁻² /30.3 mAh cm ⁻³	23.4 mAh g ⁻¹ /0.098 mAh cm ⁻² /12.3 mAh cm ⁻³
PTMA-MW15	4.11 mg cm ⁻²	111 mAh g ⁻¹ /0.456 mAh cm ⁻² /66.8 mAh cm ⁻³	99.8 mAh g ⁻¹ /0.410 mAh cm ⁻² /60.1 mAh cm ⁻³	98.1 mAh g ⁻¹ /0.403 mAh cm ⁻² /59.1 mAh cm ⁻³	91.2 mAh g ⁻¹ /0.375 mAh cm ⁻² /54.9 mAh cm ⁻³
	9.65 mg cm ⁻²	111 mAh g ⁻¹ /1.07 mAh cm ⁻² /66.8 mAh cm ⁻³	100.2 mAh g ⁻¹ /0.967 mAh cm ⁻² /60.3 mAh cm ⁻³	91.3 mAh g ⁻¹ /0.881 mAh cm ⁻² /55.0 mAh cm ⁻³	66.0 mAh g ⁻¹ /0.637 mAh cm ⁻² /39.7 mAh cm ⁻³
PTMA-MW10	3.92 mg cm ⁻²	111 mAh g ⁻¹ /0.435 mAh cm ⁻² /61.7 mAh cm ⁻³	97.0 mAh g ⁻¹ /0.380 mAh cm ⁻² /53.9 mAh cm ⁻³	92.6 mAh g ⁻¹ /0.363 mAh cm ⁻² /51.5 mAh cm ⁻³	76.8 mAh g ⁻¹ /0.301 mAh cm ⁻² /42.7 mAh cm ⁻³
PTMA-MW5	4.23 mg cm ⁻²	111 mAh g ⁻¹ /0.469 mAh cm ⁻² /63.3 mAh cm ⁻³	97.1 mAh g ⁻¹ /0.410 mAh cm ⁻² /55.4 mAh cm ⁻³	83.1 mAh g ⁻¹ /0.351 mAh cm ⁻² /47.4 mAh cm ⁻³	56.2 mAh g ⁻¹ /0.237 mAh cm ⁻² /32.1 mAh cm ⁻³
PTMA-MW2.5	4.15 mg cm ⁻²	111 mAh g ⁻¹ /0.461 mAh cm ⁻² /62.7 mAh cm ⁻³	93.2 mAh g ⁻¹ /0.387 mAh cm ⁻² /52.6 mAh cm ⁻³	75.8 mAh g ⁻¹ /0.315 mAh cm ⁻² /42.8 mAh cm ⁻³	35.6 mAh g ⁻¹ /0.148 mAh cm ⁻² /20.1 mAh cm ⁻³

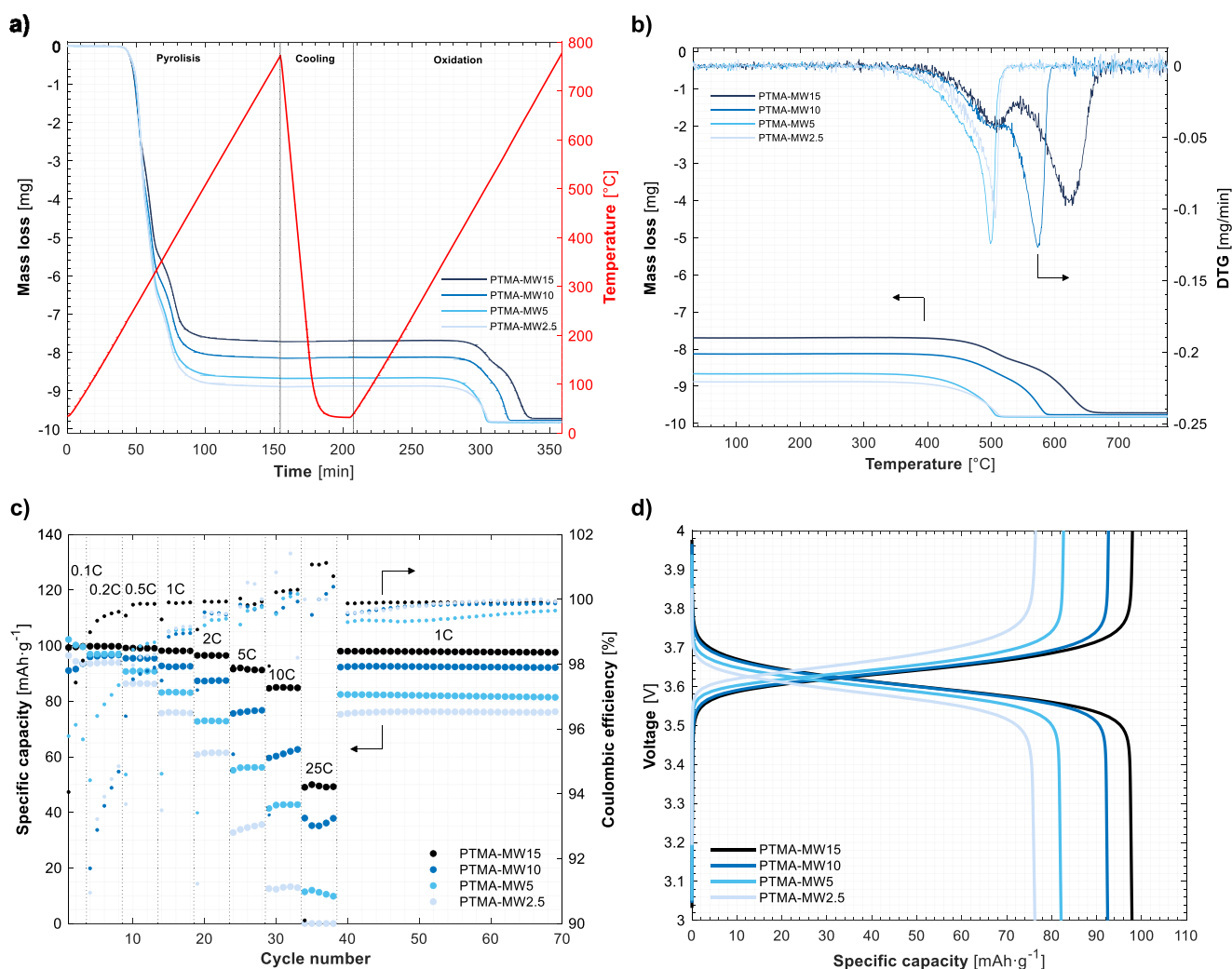


Figure 2. (a) TGA results of the PTMA-MW15, PTMA-MW10, PTMA-MW5, and PTMA-MW2.5 samples; (b) detail on the oxidation part of the TGA results on the four samples, with the respective DTG curves; (c) specific capacity and Coulombic efficiency vs cycle number for the rate performance test of the four samples in coin cells with a lithium metal anode at 20 °C; (d) related voltage vs specific capacity charge and discharge curves of the four samples at 1C (cycle no. 50 in panel c).

The electrochemical performance upon galvanostatic charge and discharge tests performed on the three materials in coin cells against lithium metal anodes is reported in Table 3, and it is shown in Figure 1c and d. PTMA-MW15 shows the highest

specific capacity and the lowest overpotential at every current rate, as it can be seen from the specific capacity trend and the voltage–capacity curves. At 1C, the specific capacity of PTMA-MW15 is 99.7 mAh g⁻¹, against 57.1 mAh g⁻¹ for PTMA-SP15

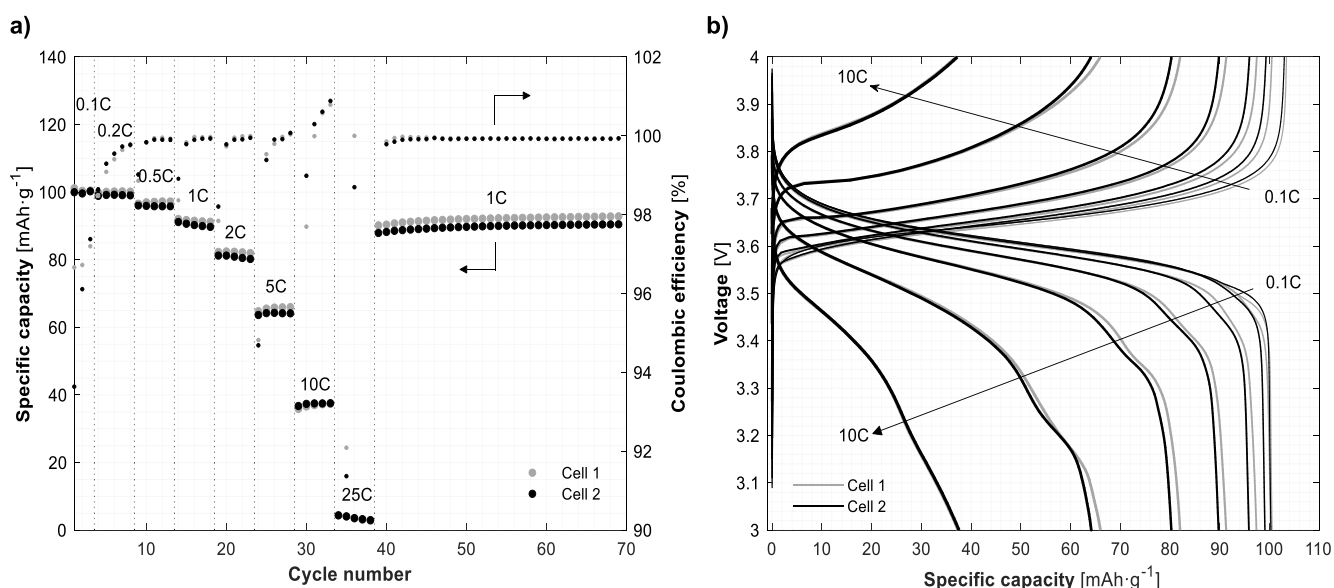


Figure 3. (a) Specific capacity and Coulombic efficiency vs cycle number for the rate performance test of the PTMA-MW15 high mass loading electrodes in coin cells with a lithium metal anode at 20 °C. (b) Related voltage vs specific capacity charge and discharge curves of the two samples at several current rates.

and 50.8 mAh g⁻¹ of PTMA-GN15. The capacity of the latter materials drops to about 23 mAh g⁻¹ at 5C, while PTMA-MW15 retains 92.4 mAh g⁻¹ (Figure S10.a). The poor performance of PTMA-SP15 and PTMA-GN15 could be explained by their lower electronic conductivity and homogeneity of the sample, which hinder access to the full material's capacity. Instead, PTMA-MW15 achieves at 1C about 90% of the theoretical specific capacity (111 mAh g⁻¹), with the 10% capacity difference probably caused by the incomplete oxidation of the polymer during the synthesis process.

The PTMA-MW15 sample was able to cycle satisfactorily with sodium metal as anode too,^{48,49} hence using sodium ions as cations in the dual-ion battery configuration. The worst rate performance and cycling stability than the lithium-based system are probably due to the lower ionic conductivity of the 1 M NaPF₆ in EC:PC 3:7 when compared to 1 M LiPF₆ in EC:DMC 1:1, and to the higher instability of sodium metal (Figure S11).^{50,51}

In accordance with the good performance shown by the PTMA-MW15 electrodes, lower multiwalled carbon nanotube amounts in the polymerization reaction were explored to increase the active material fraction in the electrodes and maximize their areal capacity. Therefore, three additional batches were synthesized, PTMA-MW10, PTMA-MW5, and PTMA-MW2.5, respectively, with 10%, 5%, and 2.5% weight fraction of multiwalled carbon nanotubes added during the synthesis with respect to the monomer precursor.

Table 1 summarizes the most relevant characteristics of these materials. The TGA curves in Figure 2a show how the mass loss during the pyrolysis phase, i.e., the one associated with polymer decomposition, increases with the PTMA fraction in the sample. The DTG curves of the oxidation phase are quite different among the four samples (Figure 2b). PTMA-MW10 still shows two peaks, with the first one corresponding to the one at a lower temperature of the PTMA-MW15, hence to the pyrolytic soot oxidation. The second peak is situated 40 °C lower than the peak of the carbon additive oxidation (Figure S2d), probably due to the heat released by the combustion of the pyrolytic soot. On the

other hand, PTMA-MW5 and PTMA-MW2.5 show only one DTG peak, making it impossible to distinguish between the mass loss due to the pyrolytic soot and the multiwalled carbon nanotubes (Figure S2e and f). The amount of polymer in these two samples was hence estimated by assuming that they have the same percentage difference between the actual and theoretical weight fractions of PTMA of the averages of PTMA-MW15 and PTMA-MW10. Overall, the actual PTMA fraction in the powders of the analyzed samples is about 2.5% lower than the desired value.

As expected, the true densities of the powders were found to be 1.227 g cm⁻³ for PTMA-MW10, 1.193 g cm⁻³ for PTMA-MW5, and 1.179 g cm⁻³ for PTMA-MW2.5. From these measurements, it is estimated that the PTMA polymer has a true density of 1.17 g cm⁻³ (see the Supporting Information for details about the PTMA density estimation, in particular, Figure S9).

By measurement of the electronic conductivity of the powders, a clear trend with the carbon fraction is evident. PTMA-MW10 achieved a value of 7.1 × 10⁻³ S cm⁻¹, PTMA-MW5 of 8.5 × 10⁻⁷ S cm⁻¹, while it was not possible to measure the conductivity of PTMA-MW2.5, being probably too insulating for such a characterization. The SEM images reflect these findings: the PTMA-MW10 powder already shows plenty of nonconductive regions, evidenced by the white regions in the image caused by the electrostatic charging of the polymer particles (Figure S6). The images of PTMA-MW5 and PTMA-MW2.5 powders are blurred because of the same effect, which is even stronger in the latter sample (Figures S7 and S8). Isolated, nonconductive particles can be seen in the images of surfaces of the electrodes made with the active materials, with the number of these particles increasing as the additive fraction decreases.

The average active material areal loading of the PTMA-MW15 sample (4.09 mg cm⁻²) only for PTMA-MW5 and PTMA-MW2.5 electrodes is rather similar, 4.09 mg cm⁻², 4.12 mg cm⁻², and 4.28 mg cm⁻², respectively, with comparable porosities but decreasing densities due to the larger polymer fraction. Instead, electrodes made with PTMA-MW10 con-

sistently show slightly lower areal loading (3.79 mg cm^{-2}) and higher porosity ($>41\%$).

The electrochemical performance of the four samples is compared in Figure 2c and reported in Table 3, showing how the carbon fraction in the material strongly affects the performance at midhigh current rates. In fact, at 0.2C the materials have a rather comparable specific capacity, while the difference becomes much more relevant at 1C and 5C. As seen in Figure 2, where the voltage-specific capacity curves at 1C are compared, the samples with a lower amount of carbon suffer from both an overpotential caused by a higher electrode resistance and diffusion limitations. In fact, EIS measurements made with a three-electrode setup on these four PTMA-based cathodes revealed that PTMA-MW5 (Figure S12c) and PTMA-MW2.5 (Figure S12d) have a much larger low-frequency impedance than PTMA-MW15 (Figure S12a), for the whole state of charge range. The impedance at low-frequency is commonly associated with the diffusion of ions in the electrolyte and in the electrode, and a high impedance in this region is connected to a “cut” in the available capacity at moderate and high current rates.^{52,53} However, the impedance of the PTMA-MW10 cell is lower than that of all the other samples (Figure S12b), which is apparently in contrast with the results from galvanostatic cycling, showing that the capacity is inferior to that of PTMA-MW15 at all the current rates. The smaller impedance may be explained by the slightly lower mass loading and higher porosity that characterize this sample, resulting from the larger ions' availability in the pores.

Since PTMA-MW15 showed the best performance at any current rate, the material was chosen to realize high areal loading electrodes ($8.40 \pm 0.32 \text{ mg cm}^{-2}$), increasing the wet coating thickness to $300 \mu\text{m}$. Furthermore, an increase of the solid content in the slurry from 40% to 45% resulted in electrodes up to 9.65 mg cm^{-2} and theoretical areal capacity $>1 \text{ mAh cm}^{-2}$. These PTMA-based electrodes had a thickness of $\sim 150 \mu\text{m}$, which is a relatively high value even compared to commercial lithium-ion battery electrodes ($30\text{--}80 \mu\text{m}$ range).⁵⁴ To the best of our knowledge, these PTMA electrodes offer the highest areal loading for lithium-based battery with organic electrolyte (see Table S7 in the Supporting Information for a detailed comparison with other works on PTMA).^{30,32,42}

The performance of two cells made with such electrodes is shown in Figure 3a and b (Cell 1: 9.65 mg cm^{-2} , Cell 2: 9.39 mg cm^{-2}). The increase in mass loading did not affect the specific capacity at low rates, but the polarization at current rates $\geq 1\text{C}$ is evident. The loss of capacity and the increased overpotential are certainly caused by the higher resistance of the thicker electrodes and the increased mass transport losses within the electrode's porosity. The higher currents cause also higher overpotentials on the lithium metal side, which contribute significantly to the loss of capacity (Figure S13). It has to be remarked that the PTMA cathodes show good cycling stability even at such high mass loadings and that most of the degradation seems to come from the effect of the lithium metal anode. With 1 M LiPF₆ in EC:DMC 1:1 the degradation is evident: in one cell the failure is probably caused by dendrite formation, as can be inferred from the irregular behavior of the Coulombic efficiency after ca. 250 cycles; in another one, strong capacity fading is observed (Figure S14a). With a modified electrolyte (1 M LiFSI in EC:DMC 1:1) the cells are able to cycle at moderate rates for hundreds of cycles. It is known that LiFSI favors the form of a more stable interphase on the lithium metal anode than LiPF₆,^{55,56} and electrodes with mass loading $>8 \text{ mg cm}^{-2}$ were tested with the

latter electrolyte and they achieved 700 cycles, the most of which at 0.9C, with low capacity fading, thanks to the cross-linking of the PTMA polymer^{30,57} and the higher stability of the interphase on the lithium metal anode (Figure S14b).

3.2. Design of a PTMA Battery: Physical Simulations and Cost and Performance Analysis. The experimental results obtained in coin cells employing PTMA cathodes give useful information regarding the use of such high areal loading organic electrodes for practical battery cells. In fact, using thick and very porous glass fiber separators and adding plenty of electrolyte in the cells solves the problem associated with the anions' involvement in the PTMA redox process. However, when the quantity of electrolyte is limited, such as when very thin commercial plastic separators with relatively low porosity are used, the cell's electrochemical performance is severely limited if a conventional 1 M electrolyte is employed. This can be seen in the charge/discharge curves shown in Figure S15, which illustrates the results of lithium metal coin cells with both low and high mass loading electrodes in combination with a $10 \mu\text{m}$ polyolefin separator. Using a minimal amount of electrolyte to wet the separator and the cathode, only 12 mAh g^{-1} are delivered at 1C for a 4.73 mg cm^{-2} cathode, and 8 mAh g^{-1} for a 9.10 mg cm^{-2} . This poor performance is due to the limited quantity of anions present in the cell, which is not sufficient to fully charge the PTMA cathode.

We then introduce a dimensionless design parameter indicating whether the quantity of anions present in the electrolyte is enough to exploit the whole capacity of the PTMA cathode (and, in general, every dual-ion battery cathode). The parameter, indicated as K , is calculated as

$$K = \frac{(c_{e,\text{ref}} - c_{e,\text{min}})}{c_{s,\text{max, pos}}} \cdot \left(\frac{L_{\text{sep}} \epsilon_{l,\text{sep}}}{L_{\text{pos}} \epsilon_{s,\text{pos}}} + \frac{\epsilon_{l,\text{pos}}}{\epsilon_{s,\text{pos}}} \right) \quad (2)$$

where $c_{e,\text{ref}}$ is the maximum salt molar concentration in the electrolyte (i.e., battery is fully discharged), $c_{e,\text{min}}$ is the minimum salt molar concentration in the electrolyte achieved upon charge, which should not be exceeded to avoid an excessive ionic conductivity and/or electrochemical stability window decrease, $c_{s,\text{max, pos}}$ is the molar concentration of active sites in the PTMA, L_{sep} and L_{pos} are, respectively, the thickness of the separator and cathode, and $\epsilon_{l,\text{pos}}$, $\epsilon_{l,\text{sep}}$, and $\epsilon_{s,\text{pos}}$ are, respectively, the volume fraction of electrolyte in the cathode (i.e., the cathode porosity) and the separator (i.e., the separator porosity), and of active material in the cathode. A metal foil, such as lithium or sodium metal, is considered as an anode; hence, the volume of the anode is not included in the formula.

If K is higher than 1, the number of anions in the electrolyte is sufficient to compensate for the positive charges generated in the cathode during the charge of the PTMA battery. On the contrary, with K lower than 1, the cathodic active material would require more anions than those available in the electrolyte. This dimensionless parameter is directly proportional to the initial electrolyte salt concentration and to the size and porosity of the separator, and it is inversely proportional to the concentration of active sites in the cathode as well as on its size and solid fraction. The derivation of K can be found in the Supporting Information.

Through this parameter, we can investigate which combinations of design parameters allow the proper functioning of a PTMA battery; i.e., enough anions are available to fully charge the cathode material without excessively depleting the salt concentration in the electrolyte. The trend of K with some design parameters is shown in Figure 4. For all of the panels, the

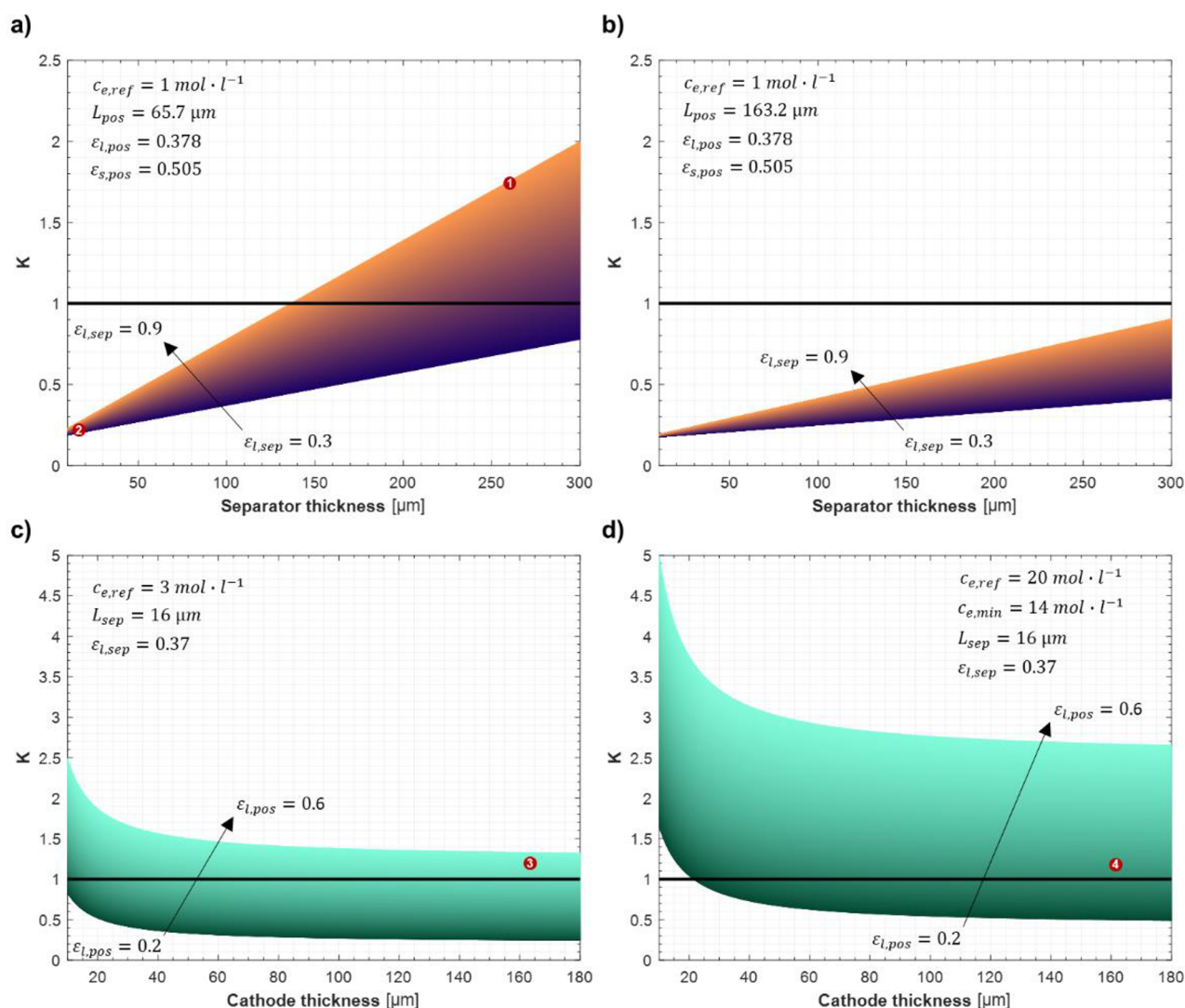


Figure 4. Study of the trend of the parameter K with (a) the separator thickness and porosity, with a lean electrolyte and a low mass loading electrode; (b) the separator thickness and porosity, with a lean electrolyte and a high mass loading electrode; (c) the cathode thickness and porosity, with a concentrated electrolyte and a thin commercial separator; and (d) the cathode thickness and porosity, with a superconcentrated electrolyte and a thin commercial separator. The red dots with the numbers inside indicate the cases that are simulated with the physical model.

value of $c_{s,max,pos}$ used to calculate K is 4.375 mol L^{-1} , which corresponds to a practical specific capacity of 100.2 mAh g^{-1} assuming the PTMA polymer density to be 1.17 g cm^{-3} .

In Figure 4a, the parameters corresponding to a low mass loading electrode (3.8 mg cm^{-2}) and 1 M electrolyte are used, and the separator thickness and porosity are varied. All the configurations below the solid black line at $K = 1$ would not completely charge the battery, while those over the line would allow the use of the full cathode capacity. From the figure it is seen as even the electrodes with the lower loading could not be fully charged without very thick and porous separator, such as the glass fiber ones used only in lab scale coin cells. Using a commercial separator, i.e., thickness $< 20 \text{ μm}$ and porosity $< 50\%$, would result in only around 20% of the battery capacity chargeable ($K \approx 0.2$).

By employing the high mass loading cathode (9.5 mg cm^{-2}) while keeping the same electrolyte concentration and volume fractions, even a separator thickness of up to 300 μm would not allow the PTMA battery to fully charge (see Figure 4b). This could come as a contradiction to our experimental results with the high mass loading electrodes, which, despite being done with

a 260 μm separator with around 90% electrolyte volume fraction, achieved full capacity at low current rates. However, in these calculations of K , we assume that the electrode and the separator have the same area, while in our coin cell setup the separator had a 16 mm diameter and the cathode 12 mm diameter, hence the separator could accommodate around the double of electrolyte than if it had the same size of the cathode.

Hence, to obtain a viable battery with such a high mass loading electrode and a thin commercial separator, assumed to have a thickness of 16 μm and a pore fraction of 37%, the concentration of the salt in the electrolyte must be substantially increased. In Figure 4c, the thickness and porosity of the cathode are varied, assuming a salt concentration of 3 mol L^{-1} (3 M), near the solubility limit of LiPF_6 in 1:1 EC:DMC at ambient temperature. By varying the cathode parameters, two contrasting effects happen: increasing the thickness of the cathode means of course having a larger amount of active material that needs to be charged, but it also means that there is more porosity in the electrode that can be exploited to accommodate electrolyte, providing additional anions for the redox process. The latter effect is more pronounced the higher the pore fraction

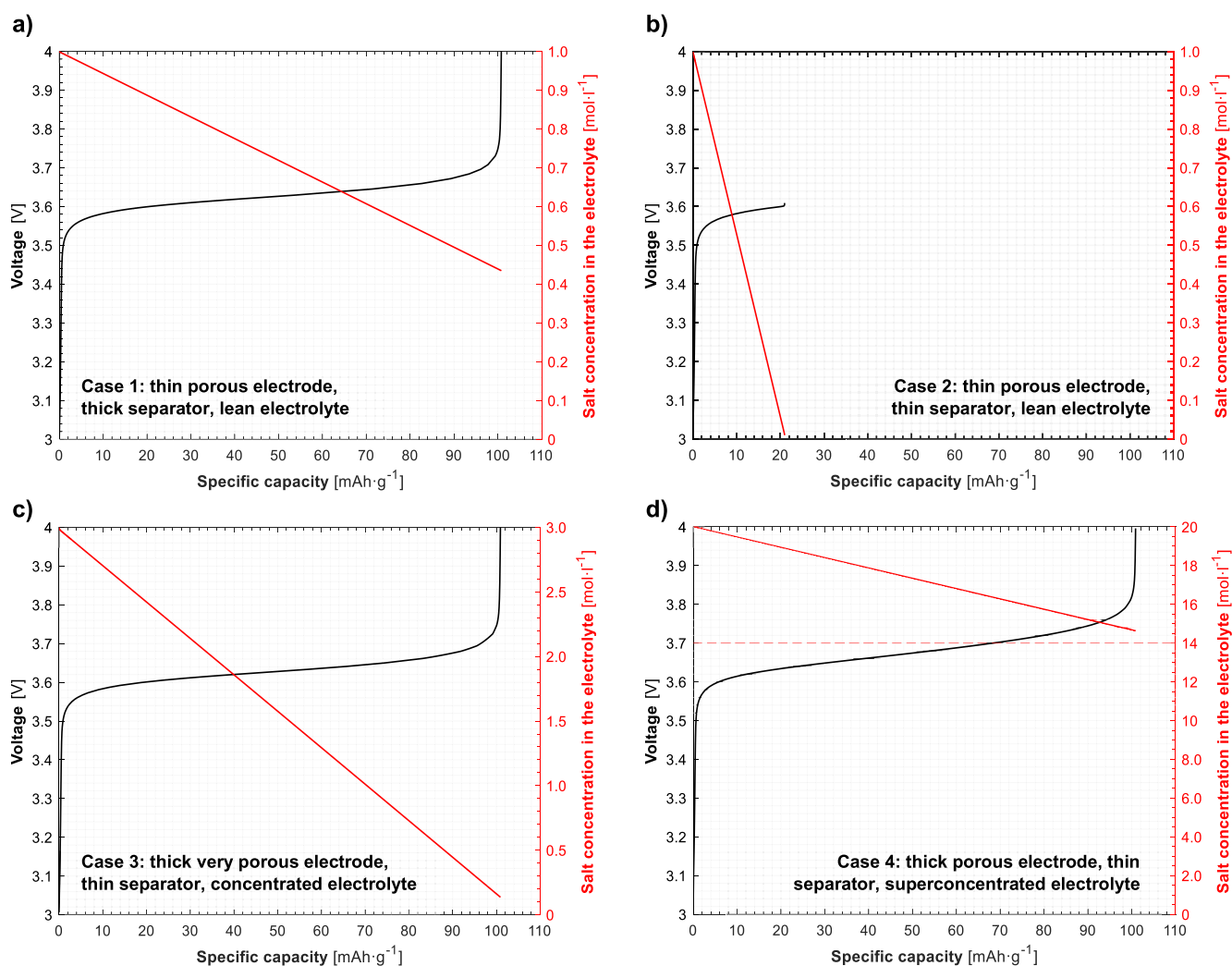


Figure 5. Voltage and electrolyte salt concentration vs specific capacity for the four simulated cases during a 0.1C charge. (a) Case 1, (b) Case 2, (c) Case 3, (d) Case 4.

of the cathode, vice versa for the former. With these parameters, the high mass loading cathodes, which have a pore fraction of around 39%, could not be fully charged. Only by increasing the cathode porosity to values higher than 50% the full chargeability is achieved. However, this modification decreases the active material electrode mass loading if the thickness is kept constant, hence the resulting mass loading and the areal capacity would be inferior to the ones of our experimental results.

Therefore, to keep the experimental cathode parameters (~ 10 mg cm $^{-2}$ PTMA electrodes and 38% porosity), the use of a hypothetical superconcentrated electrolyte must be considered, such as the 20 M LiTFSI-LiFSI in a water and acetonitrile mixture electrolyte reported in a work of Yang et al.⁵⁸ The starting concentration would be then in this case 20 mol L $^{-1}$ with the minimum concentration set to 14 mol L $^{-1}$ since an excessive decrease of the salt concentration would lead to extensive decomposition of the solvent.⁵⁸ This configuration allows full charging of the high mass loading cathode with a thickness of 163.2 μ m and a porosity of 38% with a thin commercial separator, since K is higher than 1 in the plot region corresponding to this parameter combination (Figure 4d).

Through the use of the physical model for dual-ion batteries developed in a previous work (details are given in the Supporting Information), several cases were simulated employing different

design parameters combinations of the PTMA batteries, to validate the empirical trends of K delineated in the previous paragraphs with more rigorous physics-based simulations. The four cases are indicated in Figure 4 with red dots in the region of the graphs corresponding to the chosen values of the cathode and separator geometry and electrolyte concentrations. All of the values of the model's parameters can be found in Tables S2 and S3, and the model domains in the four simulated cases are illustrated in Figure S17.

For case 1, where a low mass loading electrode (65.6 μ m thick and with 38% porosity) is coupled with a 260 μ m thick, very porous (90%) glass fiber separator⁵⁹ with a 1 M electrolyte, the battery can be fully charged up to the maximum available specific capacity, and the salt concentration in the electrolyte (measured at the cathode–current collector interface) decreases down to 0.44 mol L $^{-1}$ (Figure 5a). Due to the dependence of the electrolyte ionic conductivity with the concentration of the salt, the conductivity will drop from 10.7 mS cm $^{-1}$ at the beginning of the charge to 8.9 mS cm $^{-1}$ toward its end, hence hindering the ionic transport at high SOC. However, employing a thin commercial separator (16 μ m thick and with 37% porosity)⁶⁰ while keeping the same cathode and electrolyte (case 2), a charge capacity of only 21 mAh g $^{-1}$ is achieved before the salt concentration drops to values near zero (Figure 5b).

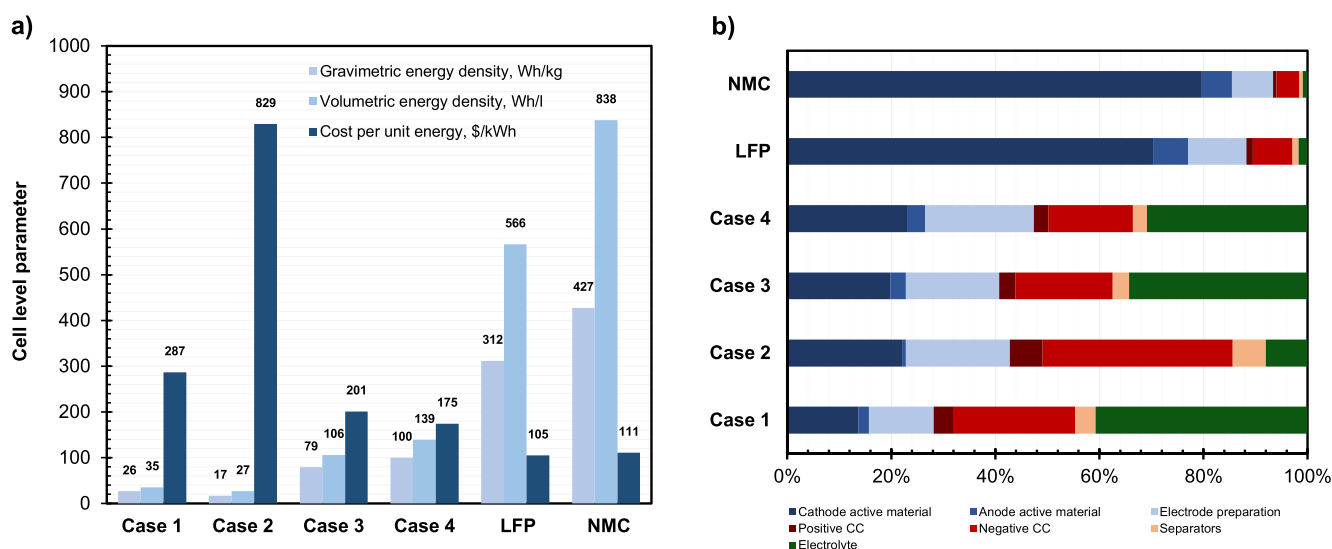


Figure 6. (a) Comparison of the gravimetric energy density, volumetric energy density, and cost per unit energy at the cell level of the simulated battery packs. (b) Cost breakdown of the materials required for the cell assembly in the simulated battery packs.

For case 3, the concentration of the lithium salt in the electrolyte is increased up to 3 mol L^{-1} , and the cathode thickness and porosity are set respectively to $162.3 \mu\text{m}$ and 54% , while keeping the same separator. With this configuration, the PTMA battery can be fully charged but the salt concentration drops to around 0.12 mol L^{-1} (Figure 5c). The ionic conductivity initially raises from 3.5 mS cm^{-1} to the maximum of 10.7 mS cm^{-1} around 70% SOC, since at very high concentrations the conductivity is lower than at the optimum around 1 mol L^{-1} , but then it sharply decreases to 4.4 mS cm^{-1} at the end of the charge.

Finally, in case 4 the use of a 20 M superconcentrated electrolyte is simulated. Due to the lack of data regarding the transport properties of such an electrolyte, a constant ionic conductivity of 5 mS cm^{-1} , a transference number of 0.5 , a diffusion coefficient of $7.5 \times 10^{-11} \text{ m}^2 \text{ s}^{-1}$, and an activity coefficient of 1 are assumed. With this theoretical electrolyte, $162.3 \mu\text{m}$ thick and 38% porosity composite PTMA electrodes, such as the high mass loading cathode presented in the experimental section, could be fully charged without exceeding the lower limit of salt concentration (14 mol L^{-1}) (Figure 5d).

The four PTMA battery cases were further analyzed from a techno-economic point of view modeling their potential cost and energy density for a domestic energy storage battery of 11.5 kWh with the comprehensive software BatPac 5.0. The sets of parameters used in the model are reported in Table S4, while the main results of the simulations are reported in Table S5 and shown in Figure 6. For the sake of comparison, results obtained by simulating lithium iron phosphate (LFP) and nickel–manganese–cobalt oxide (NMC 622) lithium metal batteries are also reported. We assumed a relatively low cost for the PTMA active material, equal to $10 \text{ \$ kg}^{-1}$, slightly inferior to the one of LFP pre-2022.^{35,61}

Case 1 achieves only 26 Wh kg^{-1} and 25 Wh L^{-1} at the cell level, for a cost of $\$287 \text{ kWh}^{-1}$, due to the very thick separator that adds inactive weight and volume to the battery and whose pores require a high amount of (expensive and heavy) electrolyte to be filled.

In case 2, where the separator is commercial, but the specific capacity of the cathode is only one-half of the regular one, the price raises to $\$829 \text{ kWh}^{-1}$, with a decrease in both gravimetric

and volumetric energy density of the cell when compared to case 1. Despite the thin separator and the much lower quantity of electrolyte in the cell, the insufficient capacity delivered by the positive electrode causes a severe increase of the area required to obtain the nominal energy throughput, hence increasing the costs mostly for active materials, separators, and current collectors.

With case 3, where a 3 M electrolyte is used together with a thicker and more porous PTMA electrode and a commercial separator, we observe a great improvement of both the gravimetric and volumetric energy density, which reach respectively 79 Wh kg^{-1} and 106 Wh L^{-1} , for a cost of $\$201 \text{ kWh}^{-1}$. The cost per liter and density of the electrolyte increase with respect to the previous two cases ($\$4.8 \text{ L}^{-1}$ and 1.2 g cm^{-3} vs $\$14.1 \text{ L}^{-1}$ and 1.4 g cm^{-3}), due to the three times higher amount of lithium salt dissolved in the solvent, but the benefits brought by the higher areal capacity of the cathode offset this effect.

Finally, we simulate case 4, with the strong assumption that a lithium metal anode could be used with such a semiaqueous superconcentrated electrolyte,⁶² and using $\$20 \text{ L}^{-1}$ and 1.7 g cm^{-3} as values for the cost and the density of the electrolyte. Compared to the previous case, the further increase of the electrode mass loading by setting the cathode porosity to 38% brings an improvement in the cell level energy densities (100 Wh kg^{-1} and 139 Wh L^{-1}) as well as the cell cost ($\$175 \text{ kWh}^{-1}$). Hence, the strategy of using highly concentrated electrolytes is confirmed to be beneficial to achieving better performing PTMA batteries, despite the higher cost and weight of the electrolyte.

Nevertheless, comparing the results of these cases with the inorganic cathodes, the commercial chemistries have 3–4 times more gravimetric energy density and 4–6 times more volumetric energy density than the best performing organic battery for a cost that is 35–40% lower. The volumetric energy density is particularly penalized because of the much lower density of PTMA (1.17 g cm^{-3}) than NMC 622 (4.65 g cm^{-3}) and LFP (3.45 g cm^{-3}).

Looking at the cost breakdown (Figure 6b), we can observe how the electrolyte is the major cost contributor in the simulated cases with organic batteries, except case 2 where the very high area required by the battery makes the cost for current collectors

dominant. The cost for the materials required for the electrode preparation has also a large impact, because of the high weight fraction of carbon and binder in the organic electrodes. Instead, in the inorganic cathode batteries, the active material cost is the most relevant contribution by far, due to the high cost per unit mass of NMC 622 and LFP set in the simulations (respectively, \$40 kg⁻¹ and \$25 kg⁻¹) and the lower relative impact of the other cost voices. The electrolyte represents a mere 1–2% cost fraction in the inorganic cathode batteries, while it is between 8% and 40% for the redox polymer batteries.

In synthesis, the energy density of inorganic cathodes seems out of reach for PTMA batteries, due to the low density of the active material, the inferior specific capacity, and the high impact of the electrolyte mass and cost. The two classes of energy storage devices are nearer, in terms of cost per kWh, but the advantage of the conventional chemistries is evident. Nevertheless, these simulations do not consider niche high-power-to-energy ratio applications, which may be more suited for an organic radical such as PTMA.

4. CONCLUSION

The study focused on the feasibility of high mass loading electrodes using a mixture of PTMA and a carbon additive and their performance as positive electrodes in Li metal batteries. The results showed that the 85% PTMA – 15% multiwalled carbon nanotubes mixture exhibited excellent performance at both low and high current rates, making it a suitable choice for high mass loading electrodes. The adjustment of the aqueous coating process allowed for viable electrodes with up to 9.65 mg cm⁻² of active material loading and a theoretical areal capacity >1 mAh cm⁻². These electrodes maintained good rate performance and cycling stability despite the large thickness.

To assess the practical implementation of such high mass loading PTMA organic batteries, simulations were conducted using different design parameters in the physical model for dual-ion batteries. It was observed that the choice of separator, electrolyte concentration, and electrode geometry significantly influenced the battery's performance. For instance, a porous glass fiber separator enabled the battery to reach its maximum specific capacity even with a 1 M electrolyte, but when a thin commercial separator was used, the battery's performance was severely limited. This limitation, characteristic of dual-ion batteries, can be mitigated by using highly concentrated electrolytes.

The study also examined the techno-economic aspects of PTMA batteries for small battery packs. Simulations with a detailed model showed that the energy density and cost of PTMA batteries may not match those of inorganic cathodes even in the most optimistic scenario.

In the synthesis, this work emphasizes the importance of a broader perspective when considering beyond laboratory-scale batteries, shedding light on the challenges associated with transferring successful results obtained under typical laboratory conditions to more realistic cell configurations.

■ ASSOCIATED CONTENT

Data Availability Statement

The data set with the cycling and impedance data used in this work can be downloaded from the Zenodo repository (10.5281/zenodo.8348589).

SI Supporting Information

The Supporting Information is available free of charge at <https://pubs.acs.org/doi/10.1021/acsami.3c11838>.

Additional physicochemical characterization data (electronic conductivity, TGA, SEM), details on the calculation of the porosity of the electrodes, additional electrochemical characterization data (battery cycling, electrochemical impedance spectroscopy), and details on the structure and the results of the physical battery model and the cost and energy density model (PDF)

■ AUTHOR INFORMATION

Corresponding Author

Stefano Passerini – Helmholtz Institute Ulm (HIU)
Electrochemical Energy Storage, Ulm 89081, Germany;
Karlsruhe Institute of Technology (KIT), Karlsruhe 76021,
Germany; Department of Chemistry, Sapienza University of
Rome, Rome 00185, Italy; orcid.org/0000-0002-6606-5304; Email: stefano.passerini@uniroma1.it

Authors

Alessandro Innocenti – Helmholtz Institute Ulm (HIU)
Electrochemical Energy Storage, Ulm 89081, Germany;
Karlsruhe Institute of Technology (KIT), Karlsruhe 76021,
Germany; Present Address: Zentrum für Sonnenenergie-
und Wasserstoff-Forschung Baden-Württemberg, Ulm
89081, Germany

Isaac Álvarez Moisés – Institute of Condensed Matter and
Nanoscience (IMCN), Université Catholique de Louvain,
Louvain-la-Neuve 1348, Belgium

Olivera Lužanin – National Institute of Chemistry, Ljubljana
1000, Slovenia; Faculty of Chemistry and Chemical
Technology, University of Ljubljana, Ljubljana 1000, Slovenia

Jan Bitenc – National Institute of Chemistry, Ljubljana 1000,
Slovenia; Faculty of Chemistry and Chemical Technology,
University of Ljubljana, Ljubljana 1000, Slovenia;
orcid.org/0000-0002-0109-8121

Jean-François Gohy – Institute of Condensed Matter and
Nanoscience (IMCN), Université Catholique de Louvain,
Louvain-la-Neuve 1348, Belgium; orcid.org/0000-0003-4169-1883

Complete contact information is available at:
<https://pubs.acs.org/10.1021/acsami.3c11838>

Author Contributions

Alessandro Innocenti: Conceptualization, Methodology, Investigation, Software, Visualization, Formal analysis, Writing—original draft. **Isaac Álvarez Moisés**: Resources, Investigation, Writing—review and editing. **Jean-François Gohy**: Resources, Writing—review and editing, Supervision, Funding acquisition. **Olivera Lužanin**: Investigation, Writing—review and editing. **Jan Bitenc**: Writing—review and editing, Supervision, Funding acquisition. **Stefano Passerini**: Conceptualization, Writing—review and editing, Supervision, Funding acquisition.

Notes

The authors declare no competing financial interest.

■ ACKNOWLEDGMENTS

All the authors acknowledge the EU's Horizon 2020 Research and Innovation programme under Marie Skłodowska-Curie Grant Agreement 860403 "POLYSTORAGE" for the funding. A.I. and S.P. acknowledge the Helmholtz Association basic

funding, too. The authors thank Po-Hua Su for the preparation of the LiFSI-based electrolyte.

REFERENCES

- (1) *Trends in Batteries – Global EV Outlook 2023*. IEA <https://www.iea.org/reports/global-ev-outlook-2023/trends-in-batteries>.
- (2) Vaalma, C.; Buchholz, D.; Weil, M.; Passerini, S. A cost and resource analysis of sodium-ion batteries. *Nat. Rev. Mater.* **2018**, *3*, 18013.
- (3) Greim, P.; Solomon, A. A.; Breyer, C. Assessment of lithium criticality in the global energy transition and addressing policy gaps in transportation. *Nat. Commun.* **2020**, *11*, 4570.
- (4) Tian, Y.; et al. Promises and Challenges of Next-Generation “Beyond Li-ion” Batteries for Electric Vehicles and Grid Decarbonization. *Chem. Rev.* **2021**, *121*, 1623–1669.
- (5) Duffner, F.; et al. Post-lithium-ion battery cell production and its compatibility with lithium-ion cell production infrastructure. *Nature Energy* **2021**, *6*, 123–134.
- (6) Esser, B.; et al. A perspective on organic electrode materials and technologies for next generation batteries. *J. Power Sources* **2021**, *482*, No. 228814.
- (7) Kim, J.; et al. Organic batteries for a greener rechargeable world. *Nat. Rev. Mater.* **2023**, *8*, 54–70.
- (8) Gupta, D.; Gupta, S. J.; Vlad, A. New avenues for organic redox materials as sustainable lithium-ion battery cathodes. *Org. Mater.* **2023**, *5*, 21–34.
- (9) Muench, S.; et al. Polymer-Based Organic Batteries. *Chem. Rev.* **2016**, *116*, 9438–9484.
- (10) Goujon, N.; Casado, N.; Patil, N.; Marcilla, R.; Mecerreyes, D. Organic batteries based on just redox polymers. *Prog. Polym. Sci.* **2021**, *122*, No. 101449.
- (11) Kye, H.; Kang, Y.; Jang, D.; Kwon, J. E.; Kim, B.-G. P-type redox-active organic electrode materials for next-generation rechargeable batteries. *Adv. Energy Sustain. Res.* **2022**, *3*, No. 2200030.
- (12) Duan, A.; Wang, Z.; Huang, X.; Li, Y. Anion-dependent redox chemistry of p-type poly(vinylidimethylphenazine) cathode materials. *Angew. Chem., Int. Ed. Engl.* **2023**, *62*, No. e202302754.
- (13) Zhang, L.; Wang, H.; Zhang, X.; Tang, Y. A review of emerging dual-ion batteries: Fundamentals and recent advances. *Adv. Funct. Mater.* **2021**, *31*, No. 2010958.
- (14) Placke, T.; et al. Perspective on performance, cost, and technical challenges for practical dual-ion batteries. *Joule* **2018**, *2*, 2528–2550.
- (15) Janoschka, T.; Hager, M. D.; Schubert, U. S. Powering up the future: radical polymers for battery applications. *Adv. Mater.* **2012**, *24*, 6397–6409.
- (16) Nishide, H. Organic redox polymers as electrochemical energy materials. *Green Chem.* **2022**, *24*, 4650–4679.
- (17) Nakahara, K.; et al. Rechargeable batteries with organic radical cathodes. *Chem. Phys. Lett.* **2002**, *359*, 351–354.
- (18) Bobela, D. C.; et al. Close Packing of Nitroxide Radicals in Stable Organic Radical Polymeric Materials. *J. Phys. Chem. Lett.* **2015**, *6*, 1414–1419.
- (19) Karlsson, C.; Suga, T.; Nishide, H. Quantifying TEMPO Redox Polymer Charge Transport toward the Organic Radical Battery. *ACS Appl. Mater. Interfaces* **2017**, *9*, 10692–10698.
- (20) Wang, S.; Li, F.; Easley, A. D.; Lutkenhaus, J. L. Real-time insight into the doping mechanism of redox-active organic radical polymers. *Nat. Mater.* **2019**, *18*, 69–75.
- (21) Easley, A. D.; et al. Nitroxide Radical Polymer–Solvent Interactions and Solubility Parameter Determination. *Macromolecules* **2020**, *53*, 7997–8008.
- (22) Kim, J.-K.; et al. Organic radical battery with PTMA cathode: Effect of PTMA content on electrochemical properties. *J. Ind. Eng. Chem.* **2008**, *14*, 371–376.
- (23) Nakahara, K.; Oyaizu, K.; Nishide, H. Electrolyte anion-assisted charge transportation in poly(oxoammonium cation/nitroxyl radical) redox gels. *J. Mater. Chem.* **2012**, *22*, 13669.
- (24) Ernould, B.; Sieuw, L.; Barozzino-Consiglio, G.; Gohy, J.-F.; Vlad, A. Negative redox potential shift in fire-retardant electrolytes and consequences for high-energy hybrid batteries. *ACS Applied Energy* **2019**, *2* (11), 7879–7885.
- (25) Gerlach, P.; Burges, R.; Lex-Balducci, A.; Schubert, U. S.; Balducci, A. Influence of the salt concentration on the electrochemical performance of electrodes for polymeric batteries. *Electrochim. Acta* **2019**, *306*, 610–616.
- (26) Nakahara, K.; et al. Al-laminated film packaged organic radical battery for high-power applications. *J. Power Sources* **2007**, *163*, 1110–1113.
- (27) Nakahara, K.; Oyaizu, K.; Nishide, H. Organic Radical Battery Approaching Practical Use. *Chem. Lett.* **2011**, *40*, 222–227.
- (28) Muench, S.; et al. Printable ionic liquid-based gel polymer electrolytes for solid state all-organic batteries. *Energy Storage Materials* **2020**, *25*, 750–755.
- (29) Wild, A.; Korell, M.; Münch, S.; Lex-Balducci, A.; Brendel, J.; Sigmar Schubert, U. Solid electrolyte for organic batteries. U.S. Patent 1637318 B2, 2023.
- (30) Vlad, A.; Rolland, J.; Hauffman, G.; Ernould, B.; Gohy, J.-F. Melt-polymerization of TEMPO methacrylates with nano carbons enables superior battery materials. *ChemSusChem* **2015**, *8*, 1692–1696.
- (31) Iwasa, S.; Nishi, T.; Sato, H.; Nakamura, S. Flexibility and high-rate discharge properties of organic radical batteries with gel-state electrodes. *J. Electrochem. Soc.* **2017**, *164*, A884–A888.
- (32) Hatakeyama-Sato, K.; Wakamatsu, H.; Katagiri, R.; Oyaizu, K.; Nishide, H. An ultrahigh output rechargeable electrode of a hydrophilic radical polymer/nanocarbon hybrid with an exceptionally large current density beyond 1 A cm⁻². *Adv. Mater.* **2018**, *30*, No. e1800900.
- (33) Molina, A.; et al. Electrode Engineering of Redox-Active Conjugated Microporous Polymers for Ultra-High Areal Capacity Organic Batteries. *ACS Energy Lett.* **2020**, *5*, 2945–2953.
- (34) Innocenti, A.; Moisés, I. Á.; Gohy, J.-F.; Passerini, S. A modified Doyle-Fuller-Newman model enables the macroscale physical simulation of dual-ion batteries. *J. Power Sources* **2023**, *580*, No. 233429.
- (35) Nelson, P. A.; Ahmed, S.; Gallagher, K. G.; Dees, D. W. *Modeling the Performance and Cost of Lithium-Ion Batteries for Electric-Drive Vehicles*, third ed.; Argonne National Lab, 2019. Retrieved from <https://www.osti.gov/biblio/1503280>.
- (36) ISO 9924–3:2009. *Rubber and rubber products — Determination of the composition of vulcanizates and uncured compounds by thermogravimetry — Part 3: Hydrocarbon rubbers, halogenated rubbers and polysiloxane rubbers after extraction*. ISO, 2020. <https://www.iso.org/standard/44151.html>.
- (37) Kim, S. H.; Mulholland, G. W.; Zachariah, M. R. Density measurement of size selected multiwalled carbon nanotubes by mobility-mass characterization. *Carbon N. Y.* **2009**, *47*, 1297–1302.
- (38) Bauhofer, W.; Kovacs, J. Z. A review and analysis of electrical percolation in carbon nanotube polymer composites. *Compos. Sci. Technol.* **2009**, *69*, 1486–1498.
- (39) Zhang, Y.; et al. Impact of the synthesis method on the solid-state charge transport of radical polymers. *J. Mater. Chem. C Mater. Opt. Electron. Devices* **2018**, *6*, 111–118.
- (40) Rostro, L.; Wong, S. H.; Boudouris, B. W. Solid state electrical conductivity of radical polymers as a function of pendant group oxidation state. *Macromolecules* **2014**, *47*, 3713–3719.
- (41) Suguro, M.; Iwasa, S.; Nakahara, K. Fabrication of a practical and polymer-rich organic radical polymer electrode and its rate dependence. *Macromol. Rapid Commun.* **2008**, *29*, 1635–1639.
- (42) Iwasa, S.; Nishi, T.; Nakamura, S. Enhancement of rapid charging capability of organic radical battery using ethylene carbonate-based electrolyte containing LiFSI. *J. Power Sources* **2018**, *402*, 157–162.
- (43) Jin, W.; et al. Radical polymer grafted graphene for high-performance Li⁺/Na⁺ organic cathodes. *J. Power Sources* **2021**, *511*, No. 230363.
- (44) Zhou, T.; et al. Radical polymer-grafted carbon nanotubes as high-performance cathode materials for lithium organic batteries with promoted n-/p-type redox reactions. *J. Power Sources* **2021**, *483*, No. 229136.

- (45) Innes, J. R.; Young, R. J.; Papageorgiou, D. G. Graphene nanoplatelets as a replacement for carbon black in rubber compounds. *Polymers (Basel)* **2022**, *14*, 1204.
- (46) Nevers, D. R.; Brushett, F. R.; Wheeler, D. R. Engineering radical polymer electrodes for electrochemical energy storage. *J. Power Sources* **2017**, *352*, 226–244.
- (47) Lain, M. J.; Brandon, J.; Kendrick, E. Design Strategies for High Power vs. High Energy Lithium Ion Cells. *Batteries* **2019**, *5*, 64.
- (48) Kim, J.-K.; Kim, Y.; Park, S.; Ko, H.; Kim, Y. Encapsulation of organic active materials in carbon nanotubes for application to high-electrochemical-performance sodium batteries. *Energy Environ. Sci.* **2016**, *9*, 1264–1269.
- (49) Hu, Y.; et al. Molecular-level anchoring of polymer cathodes on carbon nanotubes towards rapid-rate and long-cycle sodium-ion storage. *Mater. Chem. Front.* **2018**, *2*, 1805–1810.
- (50) Iermakova, D. I.; Dugas, R.; Palacín, M. R.; Ponrouch, A. On the comparative stability of Li and Na metal anode interfaces in conventional alkyl carbonate electrolytes. *J. Electrochem. Soc.* **2015**, *162*, A7060–A7066.
- (51) Morales, D.; et al. Transport studies of NaPF₆ carbonate solvents-based sodium ion electrolytes. *Electrochim. Acta* **2021**, *377*, No. 138062.
- (52) Lasia, A. Impedance of porous electrodes. In *Electrochemical Impedance Spectroscopy and its Applications*; Springer: New York, 2014; pp 203–250.
- (53) Rabissi, C.; Innocenti, A.; Sordi, G.; Casalegno, A. A Comprehensive Physical-Based Sensitivity Analysis of the Electrochemical Impedance Response of Lithium-Ion Batteries. *Energy Technology* **2021**, *9*, No. 2000986.
- (54) Zheng, J.; et al. Strategies and challenge of thick electrodes for energy storage: A review. *Batteries* **2023**, *9*, 151.
- (55) Qian, J.; et al. High rate and stable cycling of lithium metal anode. *Nat. Commun.* **2015**, *6*, 6362.
- (56) Liu, X.; Mariani, A.; Diemant, T.; Pietro, M. E. D.; Dong, X.; Kuenzel, M.; Mele, A.; Passerini, S.; et al. Difluorobenzene-based locally concentrated ionic liquid electrolyte enabling stable cycling of lithium metal batteries with nickel-rich cathode. *Adv. Energy Mater.* **2022**, *12*, No. 2200862.
- (57) Wang, S.; et al. Solution-processable thermally crosslinked organic radical polymer battery cathodes. *ChemSusChem* **2020**, *13*, 2371–2378.
- (58) Yang, D.; Watanabe, M.; Takagaki, A.; Ishihara, T. High voltage and capacity dual-ion battery using acetonitrile-aqueous hybrid electrolyte with concentrated LiFSI-LiTFSI. *J. Electrochem. Soc.* **2022**, *169*, No. 120516.
- (59) Raccichini, R.; Furness, L.; Dibden, J. W.; Owen, J. R.; García-Araez, N. Impedance characterization of the transport properties of electrolytes contained within porous electrodes and separators useful for Li-S batteries. *J. Electrochem. Soc.* **2018**, *165*, A2741–A2749.
- (60) Finegan, D. P.; et al. Characterising the structural properties of polymer separators for lithium-ion batteries in 3D using phase contrast X-ray microscopy. *J. Power Sources* **2016**, *333*, 184–192.
- (61) *Steel, Aluminum, Nickel, Rare Earth, New Energy, Copper Prices Charts and News*. Shanghai Metals Market. <https://www.metal.com/>.
- (62) Yang, C.; et al. 4.0 V aqueous Li-ion batteries. *Joule* **2017**, *1*, 122–132.